RAA 2019 Vol. 19 No. 12, 172(8pp) doi: 10.1088/1674–4527/19/12/172

http://www.raa-journal.org http://iopscience.iop.org/raa

Research in Astronomy and Astrophysics

Calibration of X-ray telescope prototypes at PANTER

Ying-Yu Liao[1,2], Zheng-Xiang Shen[1,2], Jun Yu[1,2], Qiu-Shi Huang[1,2], Bin Ma[1,2], Zhong Zhang[1,2], Xiao-Qiang Wang[1,2], Kun Wang[3], Chun Xie[4], Vadim Burwitz[5], Gisela Hartner[5], Marlis-Madeleine La Caria[5], Carlo Pelliciari[5] and Zhan-Shan Wang[1,2]

[1] Key Laboratory of Advanced Micro-Structured Materials, Ministry of Education, Tongji University, Shanghai 200092, China; *wangzs@tongji.edu.cn*

[2] Institute of Precision Optical Engineering, School of Physics Science and Engineering, Tongji University, Shanghai 200092, China

[3] School of Mechanical Engineering, Tongji University, Shanghai 200092, China

[4] Sino-German College of Applied Sciences, Tongji University, Shanghai 200092, China

[5] Max-Planck-Institute for Extraterrestrial Physics, Giessenbachstr, 85748 Garching, Germany

Received 2019 April 25; accepted 2019 June 4

Abstract We report on a ground X-ray calibration of two X-ray telescope prototypes at the PANTER X-ray Test Facility, operated by the Max-Planck-Institute for Extraterrestrial Physics, in Neuried, Germany. The X-ray telescope prototypes were developed by the Institute of Precision Optical Engineering (IPOE) of Tongji University, in a conical Wolter-I configuration, using thermal glass slumping technology. Prototype #1 with three layers and Prototype #2 with 21 layers were tested to assess the prototypes' on-axis imaging performance. The measurement of Prototype #1 indicates a Half Power Diameter (HPD) of $82''$ at 1.49 keV. As for Prototype #2, we performed more comprehensive measurements of on-axis angular resolution and effective area at several energies ranging from 0.5–10 keV. The HPD and effective area are $111''$ and 39 cm^2 at 1.49 keV, respectively, at which energy the on-axis performance of the prototypes is our greatest concern.

Key words: X-ray telescopes — thermal slumping technology — X-ray calibration — PANTER

1 INTRODUCTION

In grazing incidence X-ray observations, imaging X-ray telescopes (IXTs) employing the Wolter-I configuration and its optimized solutions have been developed for half a century. The Wolter-I configuration, consisting of a pair of coaxial and confocal paraboloid and hyperboloid mirrors, was proposed by Wolter (1952a). X-ray telescopes using focusing grazing incidence optics, such as the Wolter-I configuration, were noted by Giacconi & Rossi (1960). To obtain large collecting area, a multi-layer nested Wolter-I configuration was described by Van Speybroeck & Chase (1972). To improve the angular resolution of the X-ray telescope, many optimization solutions were proposed, among which were the Wolter-Schwarzschild geometry (Wolter 1952b), polynomial geometry (Werner 1977; Burrows et al. 1992; Conconi & Campana 2002), double hyperboloid geometry (Thompson et al. 1999; Harvey et al. 2001) and Modified Wolter-Schwarzschild geometry (Saha et al. 2014). To reduce the difficulty and cost of mirror fabrication, the conical Wolter-I configuration was put forward in the 1980s (Petre et al. 1985; Serlemitsos 1988). In recent years, two optimization solutions were proposed by the Institute of Precision Optical Engineering (IPOE), which are a hybrid and a sectioned configuration (Chen et al. 2016; Liao et al. 2019). The hybrid configuration consists one conical surface and one quadratic surface, while the sectioned configuration is based on a conical Wolter-I configuration with sectioned secondary mirrors. China has made great progress in the field of non-IXTs, as demonstrated by the well-known *Hard X-ray Modulation Telescope* (*Insight-HXMT*) (Li et al. 2017). However, until now China has been involved in international cooperation to fabricate an imaging X-ray telescope with the Wolter-I configuration. In the past decade, several IXT missions have been proposed, in which China is involved. The *X-ray Timing and Polarization* (*XTP*) (Dong 2014) that was transformed

Table 1 Characteristics of Prototype #1 and #2

	Prototype #1	Prototype #2
Number of layers N	3	21
Focal length f (mm)	2052.5	2052.5
Diameter D (mm)	104–109	104–150
Mirror length L (mm)	100	100
Mirror thickness t (mm)	0.3	0.3
Mirror coating	Pt	C/Ni/Pt
Grazing angle α (deg)	0.365–0.379	0.365–0.522
HPD ($''$)	82 at 1.49 keV	111 at 1.49 keV
Effective area (cm^2)	-	39 at 1.49 keV

into the *enhanced X-ray Timing and Polarimetry* (*eXTP*) (Zhang et al. 2016), now in Phase B, is a mission that has been selected as a successor for *Insight-HXMT*. A different mission, the *Einstein Probe* (*EP*) (Yuan et al. 2015), also in Phase B, is designed to discover transients and monitor variable objects in the 0.5–4 keV X-ray band, at a sensitivity higher by one order of magnitude than those of missions currently in orbit. The *Hot Universe Baryon Survey* (*HUBS*) mission (`http://hubs.tongji.edu.cn/index.php?classid=5202`) is being proposed to primarily address the issue of "missing baryons" in the local universe.

At the IPOE of Tongji University, we have been developing imaging X-ray telescopes independently for over a decade (Wang et al. 2014; Shen et al. 2018). Thermal slumping technology is utilized to fabricate mirror substrates, which was firstly proposed in an experimental Kirkpatrick-Baez (KB) telescope for the extreme ultraviolet (EUV) and soft X-ray bands (Labov 1988), and developed for *HEFT* and *NuSTAR* optics (Craig et al. 2011; Koglin et al. 2004). Two slumped glass prototype optics modules that we fabricated were tested at the PANTER X-ray Test Facility, Prototype #1 with three mirror layers and Prototype #2 with 21. Both of them use the conical Wolter-I configuration, as illustrated in Figure 1. The confocal and concentric layers share a common focal length f, which is defined as the axial distance from the focus to the mid-point (principal plane) between the primary and secondary mirrors. The mirrors are nested tightly to maximize their on-axis collecting area. The prototype mirror module consists of six sectors, Sectors A-F, each of which rely on five graphite spacers to stack the mirrors from the mandrel shell by shell. In Table 1, the characteristics of these two prototypes are summarized.

Prototype #1 has a better Half Power Diameter (HPD), benefiting from smaller diameter. Prototype #2 with more nested mirrors was tested more comprehensively to assess the on-axis imaging performance, thus acquiring reliable feedbacks to improve the fabrication of the IXT.

2 MEASUREMENT SETUP

The PANTER X-ray Test Facility (Freyberg et al. 2005, 2008) was built to develop and characterize *ROSAT* optics. It is a laboratory operated by the Max-Planck-Institute for Extraterrestrial Physics (MPE). PANTER has been utilized successfully for developing and calibrating X-ray astronomical instrumentation for observatories such as *EXOSAT*, *Chandra* (LETG), *BeppoSAX*, *XMM-Newton*, *Swift* (XRT), *eROSITA*, etc., in addition to ROSAT. PANTER has a beam path length of 123.6 m, thereby providing a wide aperture quasi-parallel X-ray beam. This long beam length is realized by utilizing a vacuum tube (length of 120 m and diameter of 1 m) between the X-ray source and the instrument chamber (length of 12 m and diameter of 3.5 m). The instruments in the chamber can be translated and rotated by means of manipulators driven by stepper motors with a typical accuracy of $<3\,\mu$m. In the tube and chamber, the vacuum degree can be kept at a pressure of $< 10^6$ mbar during measurement. A schematic of the PANTER X-ray Test Facility is shown in Figure 2.

A dedicated backside illuminated PN-CCD camera is utilized, called Third Roentgen Photon Imaging Counter (TRoPIC) (Burwitz et al. 2013), was specially developed for calibration measurements of *eROSITA*. TRoPIC has a pixel size of 75 μm and an array of 256$\times$256 pixels, giving it a field of view of 19.2 mm$\times$19.2 mm. In front of the prototypes, a movable mask is installed, determining which sector of the optics are illuminated. For both prototypes, we intentionally fabricated one of the six sectors using mirrors with the best quality and another one with the worst quality. As for the figure error of mirrors, we utilized a linear variable differential transformer (LVDT) to make dense azimuthal and axial scans of the mirror segment surface height profile during Prototype assembly. As a result, Sector A' of Prototype #1 has the best quality. For Prototype #2, likewise, Sectors A, B and C are characterized by the best, worst and moderate quality, respectively. To study both global and local performance of the two prototypes, the four sectors mentioned earlier are tested specifically in addition to the full aperture of prototypes. The point spread function (PSF) of Prototype #1 was measured at 1.49 keV and 8.04 keV. More comprehensively, the PSF and effective area of Prototype #2 were determined at several energies, 525 eV, 1.49 keV, 4.51 keV, 4.9 keV, 8.04 keV and 9.9 keV.

As a prerequisite for reliable measurement, X-ray alignment of Prototype and the optical axis should be performed carefully. The Burkert test (Menz et al. 2013) is an efficient alignment method at PANTER, by utilizing the different behaviors of the single-reflection and double-

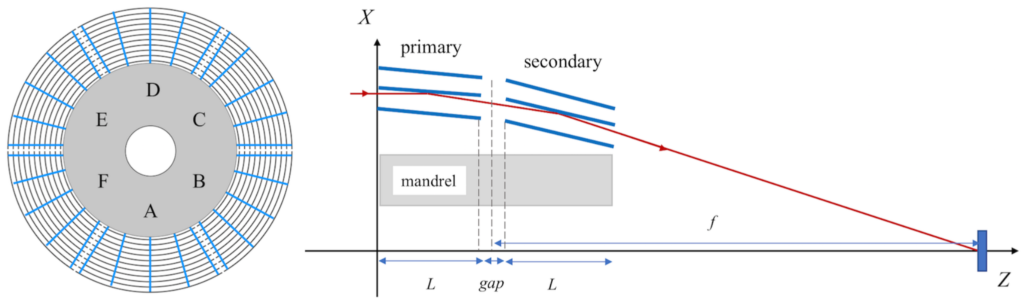

Fig. 1 Schematic of the prototype, the entrance aperture (*left*) and the cross-section profile (*right*).

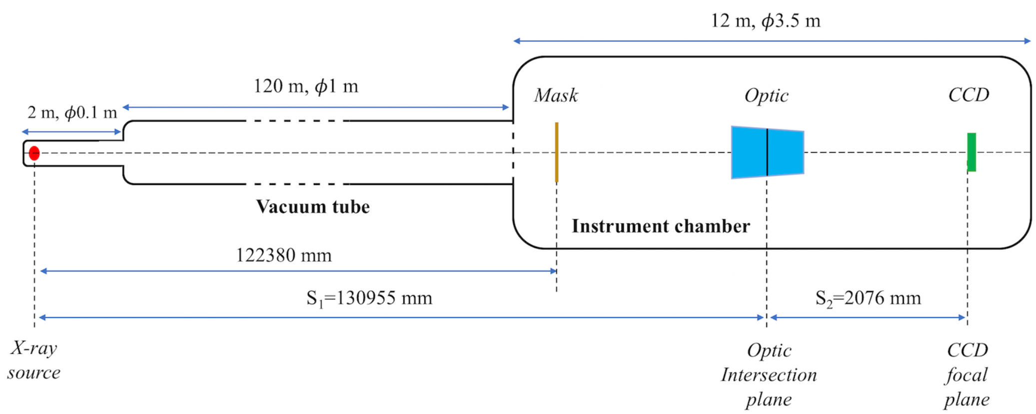

Fig. 2 Schematic of the PANTER X-ray Test Facility, where the quasi-parallel X-ray beam is achieved.

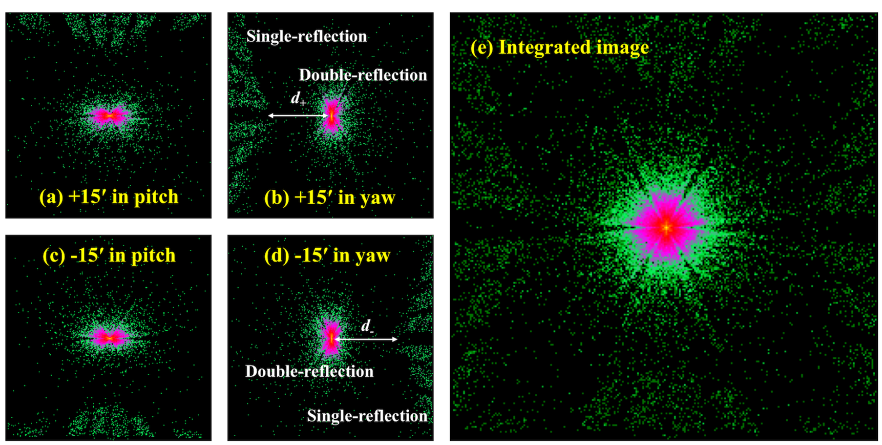

Fig. 3 Images of Prototype #2 by the Burkert test. The panels in Fig. 3(a), 3(b), 3(c) and 3(d) display the individual images and Fig. 3(e) is the integrated image.

reflection with respect to the off-axis angle, with the optic changing its attitude in pitch and yaw direction. Rays from the double-reflection contribute to the image on the focal plane, while the single-reflection is reflected only once, either by the primary mirror or the secondary mirror. The position of the image depends on the chief ray, which is determined by the source and the center of the optic. For a fixed source, the chief ray does not change as the attitude of the optic changes. As a result, the centroid of the image is also unchanged on the focal plane ideally, even though its shape changes. In other words, the position of the normal image on the focal plane is in general independent of the off-axis angle, but the position of the single-reflection is sensitively dependent on the off-axis angle. Therefore, the distance between the single-reflection and double-reflection can be significant at a large off-axis an-

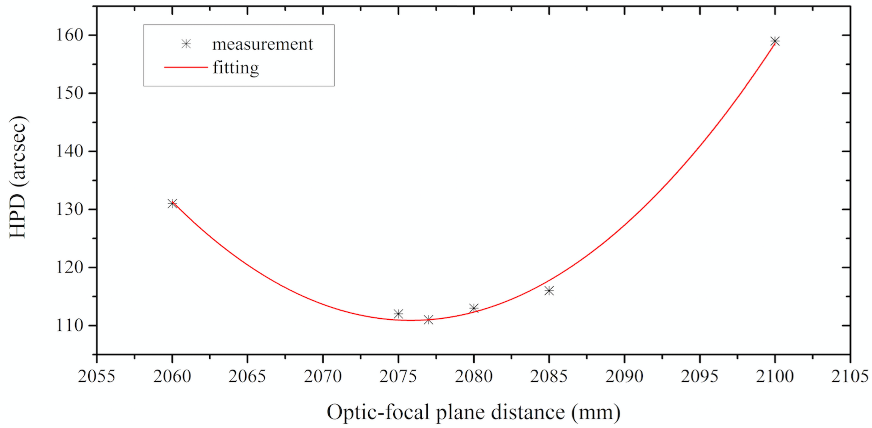

Fig. 4 Variation of HPD for Prototype #2 with focal plane distance at 1.49 keV, indicating the best focus is at a focal plane distance of 2076 mm.

gle. In addition, in the case of perfect alignment, the distances should be identical at a pair of opposite off-axis angles because of symmetry. We define the distance between the single-reflection and double-reflection as $d+$ in the case of off-axis angle of θ, and then rotate the optical path in the opposite direction to acquire $d-$ at $-\theta$ off-axis angle. In an iterative process, we adjust the attitude of the optic until the equation $d+ = d-$ makes sense. This process will provide $<1'$ knowledge of the pitch and yaw for the optic, which is far smaller than the grazing angle of the optic. Prototype #2 was finely aligned by applying the Burkert test. The images of Prototype #2 at opposite off-axis angles in pitch and yaw directions by the Burkert test are featured in Figure 3. The images were taken when the optical path was set at four equally sized and opposite off-axis angles θ, which were $\pm 15'$ in yaw and pitch directions, respectively.

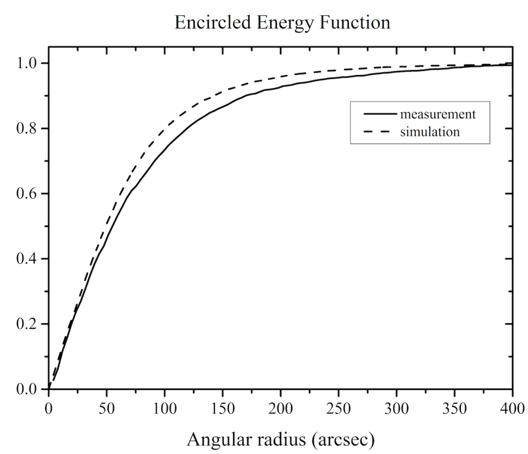

Fig. 5 Simulated and measured EEFs of Prototype #2, indicating a simulated HPD of 101″and a measured HPD of 111″.

3 MEASUREMENT RESULTS

3.1 Focus Search of Prototype #2

As shown in Figure 2, with a finite source distance S_1 the image (focal plane) distance S_2 will be slightly longer than the nominal focal length f, as expressed by the thin lens equation

$$\frac{1}{S_1} + \frac{1}{S_2} = \frac{1}{f}\,. \tag{1}$$

A process to search for the focus was performed at 1.49 keV, by adjusting the focal plane distance to determine the minimum HPD as plotted in Figure 4. The theoretical image distance is 2085 mm, while the measured image distance was slightly shorter, having a value of 2076 mm according to the best fit to the focus curve. The minimum HPD of 111″ at 1.49 keV is determined at the best focal-plane distance of 2076 mm, indicating the measured Encircled Energy Function (EEF) in Figure 5, with the simulated EEF for comparison. The preliminary assessment by means of a ray-tracing program predicted an HPD of 101″ for the prototype. In addition to the 3.9′ divergence of the X-ray beam, the figure error of every individual mirror (30″–180″) and the residual 30″ misalignment after alignment were also taken into account in the simulation. The 3.9′ beam divergence is the angular diameter of the incident beam (150 mm in diameter) with respect to the source distance (130 955 mm). The figure error of the mirrors was evaluated by an LVDT, which is an in-situ measurement system utilized to measure the mounted mirrors during the assembly process (Koglin et al. 2011). The values of 30″–180″ are used to assess the figure error of each mirror, which are the predicted results by the ray-tracing program. These results are based on the combination of one mirror with measured figure error, and another mirror in a ideal conical approximation geometry.

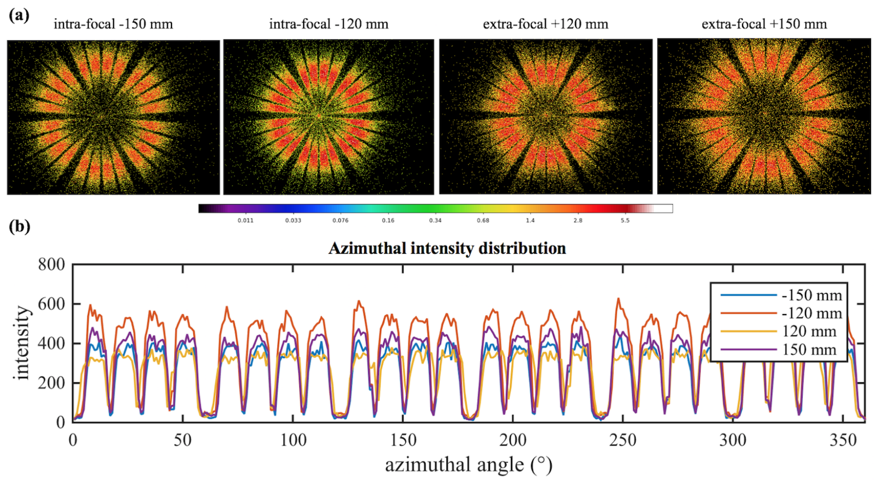

Fig. 6 (a) Out-of-focus rings of Prototype #2, intra-focal case (–120 mm, –150 mm) and extra-focal case (+120 mm, +150 mm). (b) Azimuthal intensity distribution of the out-of-focus rings.

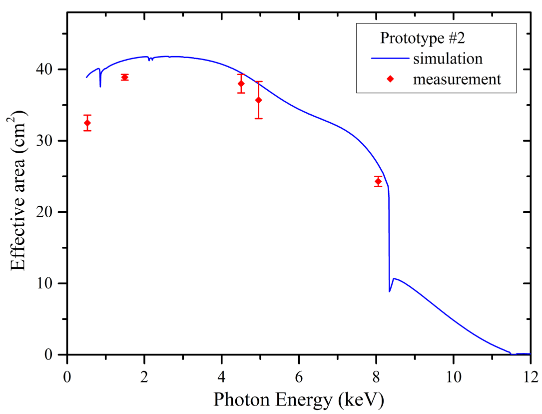

Fig. 7 Comparison of simulated and measured effective area of Prototype #2. The measured effective area at 1.49 keV deviates from the expectation by 5% as a result of epoxy glue.

The deviation of the image distance can be attributed to a combination of imperfect mirrors and small errors in the mirror assembly process. These are the issues that will be improved in the future fabrication processes. As a result of the longitudinal deformation of the mirrors and the assembly errors, the kink angle (which is theoretically twice the grazing angle) between the primary and secondary mirrors could vary. The deviation could change the image distance but would not change the PSF significantly, because the small deviation is negligible compared with the grazing angle. Approximately, a 28″ deviation in the kink angle could introduce a 9 mm deviation in the image distance, estimated by Equation (2), where α is the grazing angle, β is the deviation of the kink angle and f is the focal length

$$\Delta = f \cdot (1 - \frac{\tan(4\alpha)}{\tan(4\alpha + 2\beta)})\,. \tag{2}$$

3.2 Out-of-focus Rings of Prototype #2

Measurements of the out-of-focus rings (Misaki et al. 2008) were performed by moving the detector to positions of ±150 mm and ±120 mm from the best focus. In Figure 6, the out-of-focus rings of Prototype #2 and the azimuthal intensity distribution therein are clearly visible, as are the shadows of the support structure and graphite spacers (the entrance aperture of Prototype #2 is illustrated in Fig. 1).

By means of an out-of-focal test, the rings can be analyzed quantitatively with radial profiles to assess the local performance of the optics, which means the assessment of the local performance can be made by full illumination rather than by pencil beam. The rings are also utilized to determine the effective area, thus avoiding detector pile-up effects. The effective area was measured at 525 eV, 1.49 keV, 4.51 keV, 4.9 keV and 8.04 keV, compared with results from simulation (see Fig. 7). The effective area is derived using Equation (3), where EA represents effective area, and A and B are the photon counting rates with and without the associated optics, respectively. S is the geometric area of the detector CCD, and C is the correction factor determined by the time-stability of the X-ray beam. The time-stability was acquired by measuring the direct beam before and after the effective area test of each energy using TRoPIC. The intensity of the beam is considered to be uniform because the X-ray beam at PANTER has good uniformity. As displayed in Figure 8, the uniformity test of the X-ray beam was performed by measuring the direct beam using TRoPIC. Each square corresponds to one field of view of TRoPIC.

$$\mathrm{EA} = \frac{A}{B} \times S \times C\,. \tag{3}$$

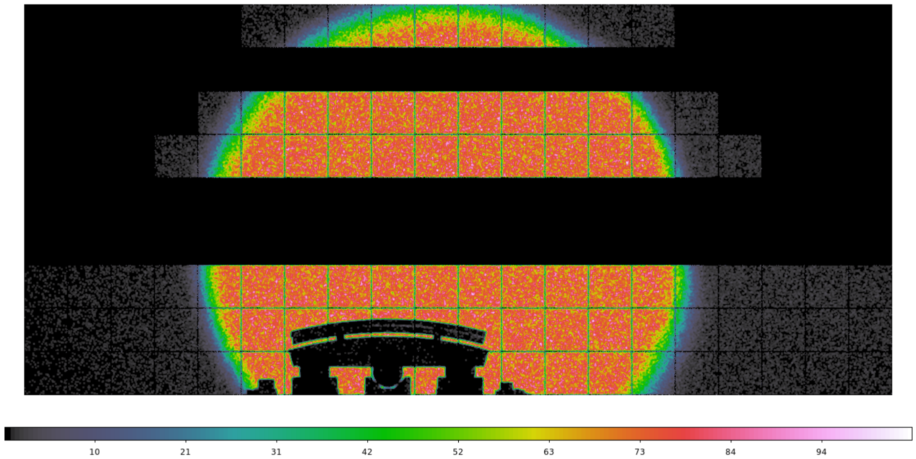

Fig. 8 Uniformity test result of the X-ray beam using TRoPIC (credit: Gisela Hartner, the PANTER X-ray Test Facility).

Table 2 Characteristics of Prototypes #1 and #2

	Energy	Prototype #2 HPD ($''$)	Prototype #1 HPD ($''$)	Prototype #2 EA (cm^2)
Full illumination	525 eV	-	-	33
	1.49 keV	111	82	39
	4.51 keV	106	-	38
	8.04 keV	99	-	23
	9.9 keV	93	-	-
Sector A (A')	1.49 keV	109	67	-
	8.04 keV	96	65	-
	1.49 keV	93	-	-
Sector B	1.49 keV	115	-	-
Sector C	1.49 keV	115	-	-

The measured effective area at 1.49 keV is 39 cm^2, our reference energy for the on-axis performance of the prototypes. This value is about 5% lower than expected, which is mainly ascribed to the epoxy glue blocking the light path. The epoxy glue is applied to bond the mirrors and graphite spacers, a few (visibly 0.2–0.3 mm in width) of which spilled out and contaminated the mirrors during the epoxy pasting and curing process. In this case, the excess epoxy glue can degrade the effective area. As demonstrated in Figure 6, the out-of-focus rings indicate a lower intensity of the area close to the graphite spacers.

Apart from the Burkert test, there are two other methods for X-ray alignment that are employed at PANTER, Cross-scan and the Egger-Menz tests (Menz et al. 2013). Cross-scan is based on symmetry of the image blurring behavior for increasing off-axis angles, which is measured by the HPD of the point image. The Egger-Menz test symmetrizes the azimuthal intensity distribution that yields symmetric effective areas. Compared with the Burkert test, Cross-scan and the Egger-Menz test are more precise but also time-consuming. Nevertheless, the Egger-Menz method can be utilized to assess the alignment of the mirrors based on the out-of-focus rings. The Egger-Menz test is designed as a fine alignment process using the symmetry of effective areas. In other words, for a perfectly aligned mirror the azimuthal intensity distribution of the effective area is homogeneous, but for an off-axis aligned mirror, the intensity distribution becomes elliptical. According to the out-of-focus rings, the azimuthal intensity is integrated, thus acquiring the azimuthal intensity distribution in Figure 6(b). Learning from the Egger-Menz method, the azimuthal intensity distribution is analyzed based on the Fast Fourier Transform, the result of which is depicted in Figure 9. By employing a low-pass filter, the shadows of the support structure and graphite spacers are removed. After that, the intensity distribution exhibits only minor variation of less than 3% in azimuth, which indicates the mirrors are aligned well.

3.3 Measurement of Prototype #1

Likewise, the smallest PSF of Prototype #1 was found at an image distance of 2080 mm. The simulated and measured EEFs of Sector A' and full aperture of Prototype #1 are plotted in Figure 10.

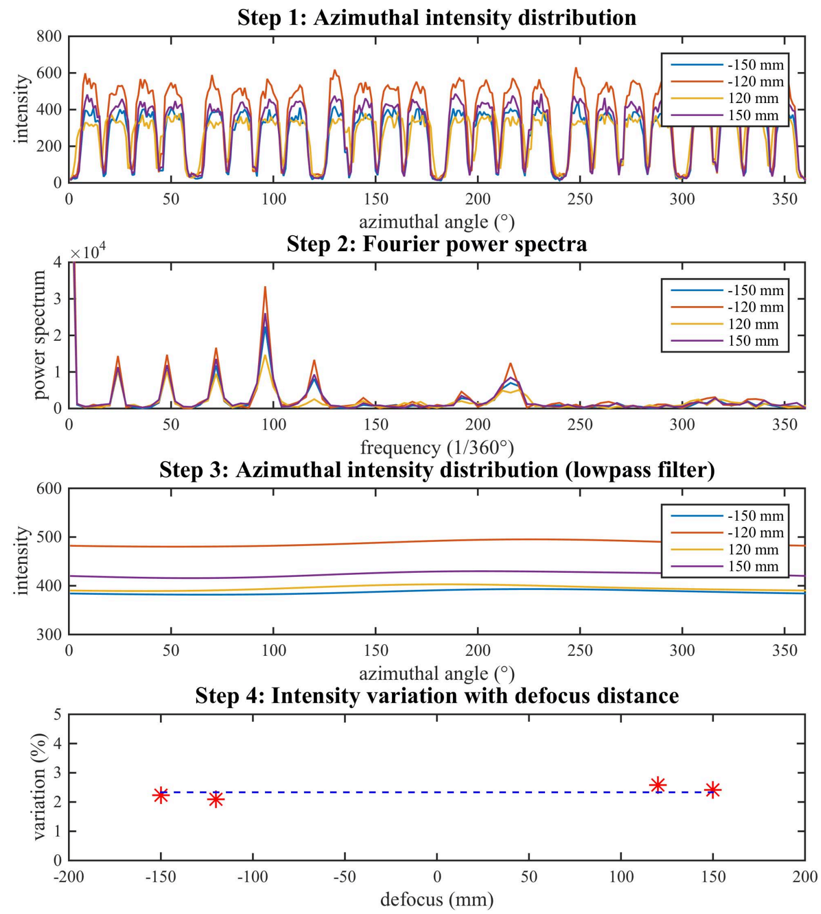

Fig. 9 Analysis of the azimuthal intensity of the out-of-focus rings, indicating minor changes of $<3\%$ in the azimuthal intensity distribution.

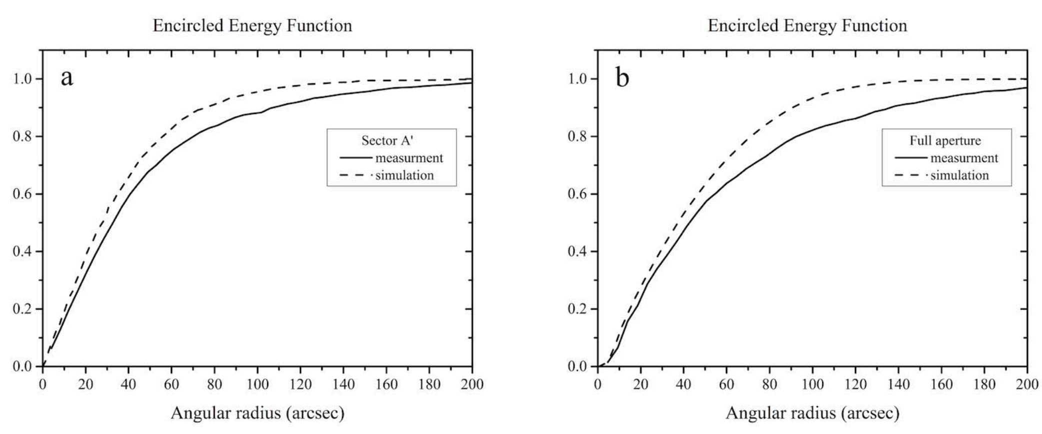

Fig. 10 (a) Simulated and measured EEFs of Sector A' of Prototype #1, indicating an HPD of 56″ and 67″ at 1.49 keV, respectively. (b) Simulated and measured EEFs of the full aperture of Prototype #1, indicating an HPD of 77″ and 82″ at 1.49 keV, respectively.

3.4 Overview of the Measurement Results

The measurement results of Prototype #1 and #2 are summarized in Table 2. The systematic error of the HPD is 4″ according to the characterization of TRoPIC, while the random error is negligible compared with the systematic error.

The prototype has a smaller HPD at higher energy because the figure error dominates the PSF test instead of the surface micro-roughness at an energy range of 0.5–10 keV for the tested prototype. In other words, outer layers, corresponding to larger HPD compared with inner layers, contribute less photons at higher energy. For the prototype at 0.5–10 keV, this makes the HPD smaller and this improvement outweighs the degradation in HPD because of X-ray scattering that results from surface micro-roughness.

4 SUMMARY

IXTs have been developed at the IPOE of Tongji University for more than a decade. Currently, thermal slumping technology is used to fabricate mirror substrates. Two X-ray mirror module prototypes assembled at IPOE, based on a conical Wolter-I configuration, were tested and calibrated at the PANTER X-ray test facility. For Prototype #1 with three layers, the HPD was determined to be 82″ at 1.49 keV. For Prototype #2 with 21 layers, the comprehensive measurements at several energies were performed to assess the on-axis imaging performance. At our main energy of interest, 1.49 keV (Al-K), measurements of Prototype #2 give an on-axis HPD of 111″ and an effective area of 39 cm^2. The measurements at PANTER indicated a reliable prediction of the prototype performance by combining the mirror figure evaluation by the LVDT and the simulation by ray-tracing program, which provided us with valuable feedback to help improve the development of our IXTs.

Acknowledgements This work was supported by the National Natural Science Foundation of China (Grant Nos. U1731242 and 61621001), and Strategic Priority Research Program of the Chinese Academy of Sciences (Grant Nos. XDA15010400 and XDA04060605).

References

Burrows, C. J., Burg, R., Giacconi, R. 1992, Astrophys. J. 392, 760
Burwitz, V., Bavdaz, M., Pareschi, G., et al. 2013, Proc. SPIE, 8861, 88611J
Chen, S.-H., Ma, S., & Wang, Z.-S. 2016, Chin. Opt. Lett. 14(12), 12340, `http://www.opticsjournal.net/Articles/Abstract?aid=OJ170111000131bIeKhN`
Conconi, P., & Campana, S. 2002, Astron. & Astrophys. 372, 1088
Craig, W. W., An, H., Blaedel, K. L., et al. 2011, Proc. SPIE, 8147, 81470H
Dong, Y. 2014, Proc. SPIE, 9144, 91443
Freyberg, M. J., Brauninger, H., Burkert, W., et al. 2005, Experimental Astronomy, 20, 405
Freyberg, M. J., Budau, B., Burkert, W., et al. 2008, Proc. SPIE, 7011, 70112T
Giacconi, R., & Rossi, B. 1960, Journal of Geophysical Research, 65, 773
Harvey, J. E., Krywonos, A., Thompson, P. L., & Saha, T. T. 2001, Appl. Opt. 40, 136
Koglin, J. E., Chen, C. M. H., Chonko, J. C., et al. 2004, Proc. SPIE, 5488, 856
Koglin, J. E., An, H., Barrire, N., et al. 2011, Proc. SPIE, 8147, 81470J
Labov, S. E. 1988, Appl. Opt. 27, 1465
Li, T.-P., Xiong, S.-L., Zhang, S.-N., et al. 2017, Sci. China-Phys. Mech. Astron. 61, 031011
Liao, Y.-Y., Shen, Z.-X., & Wang, Z.-S. 2019, J. Astron. Telesc. Instrum. Syst. 5, 014004
Menz, B., Brauninger, H., Burkert, W., et al. 2013, Proc. SPIE, 8861, 88611I
Misaki, K., Freyberg, M. J., Friedrich, P., et al. 2008, Proc. SPIE, 7011, 70112Z
Petre, R., & Serlemitsos, P. J. 1985, Appl. Opt. 24, 1833
Saha, T. T., Zhang, W. W., & McClelland, R. S. 2014, J. Astron. Telesc. Instrum. Syst., 9144, 914418
Shen, Z.-X., Yu, J., Ma, B., et al. 2018, Proc. SPIE, 10699, 106991B
Serlemitsos, P. J. 1988, Appl. Opt. 27, 1447
Thompson, P. L., & Harvey, J. E. 1999, Proc. SPIE 3766, 162
VanSpeybroeck L. P. & Chase R. C. 1972, Appl. Opt. 11, 440
Wang, Z.-S., Shen, Z.-X., Mu, B.-Z., et al. 2014, Proc. SPIE, 9144, 91441E
Werner, W. 1977, Appl. Opt. 16, 764
Wolter, V. H. 1952, Ann. Phys. 10, 94
Wolter, V. H. 1952, Ann. Phys. 10, 286
Yuan, W.-M., Zhang, C., Feng, H., et al. 2015, Huazhong Univ. Sci. Tech. J. 23(4), 383, `https://arxiv.org/abs/1506.07735v2`
Zhang, S.-N., Feroci, M., Santangelo, A., et al. 2016, Proc. SPIE, 9905, 99051